ADVANCED
FUNCTIONAL
MATERIALS

www.afm-journal.de

Materials
Views

www.MaterialsViews.com

FULL PAPER

A Solution-Processed MoO$_x$ Anode Interlayer for Use within Organic Photovoltaic Devices

Jacek J. Jasieniak, Jason Seifter, Jang Jo, Tom Mates, and Alan J. Heeger*

A simple, solution-processed route to the development of MoO$_x$ thin-films using oxomolybdate precursors is presented. The chemical, structural, and electronic properties of these species are characterized in detail, within solution and thin-films, using electrospray ionization mass spectrometry, grazing angle Fourier transform infrared spectroscopy, thermogravimetric analysis, atomic force microscopy, X-ray photoelectron spectroscopy, and ultraviolet photoelectron spectroscopy. These analyses show that under suitable deposition conditions the resulting solution processed MoO$_x$ thin-films possess the appropriate morphological and electronic properties to be suitable for use in organic electronics. This is exemplified through the fabrication of poly(3-hexylthiophene):[6,6]-phenyl C$_{61}$ butyric acid methyl ester (P3HT:PC$_{61}$BM) bulk heterojunction (BHJ) solar cells and comparisons to the traditionally used poly(3,4-ethyldioxythiophene)/poly(styrenesulfonate) anode modifying layer.

1. Introduction

The development of appropriate electron and hole charge blocking and transport layers is paramount to the fabrication of more efficient solution processed optoelectronic devices such as organic photovoltaic cells (OPVs) and light-emitting diodes (OLEDs).[1–2] The role of such layers is to create asymmetrical interfaces with respect to charge injection and collection. In OPVs,[1] this asymmetry enables reduced recombination of photogenerated electrons and holes at the electrodes, while in OLEDs,[2] it enables specific control of the spatial distribution and density of carriers in a device. The importance of such modifying layers in governing the interfacial and bulk electronic properties in these devices highlights that their degradation will have an adverse influence on device performance. Thus, only materials with suitable electronic properties and long term

stability can be considered useful for the development of such layers.

The original works on OPVs[3–5] and OLEDs[6,7] utilized bare indium tin oxide (ITO) electrodes as the anode and low work function metals (e.g., Ca, Ba or Al) as the cathode. It was quickly realized that in these proof-of-concept devices, the low work function and interfacial instability of the ITO were limiting factors for achieving high device performance.[8,9] The deposition of poly(3,4-ethylenedioxythiophene): poly(styrenesulfonate) (PEDOT:PSS), a highly conductive polymer, as an interlayer on the ITO, was subsequently shown to result in a more stable interface.[10,11] Advantageously, the higher work function of the PEDOT:PSS (5.2 eV) compared to ITO (4.8 eV) was also found to facilitate better hole injection into poly(2-methoxy-5-(2′-ethylhexyloxy)-1,4-phenylenevinylene (MEH-PPV) (ionization energy at 5.1 eV),[10,12] thus permitting higher external quantum efficiencies for electroluminescence to be realized.

Maximizing the internal electric field through the formation of ohmic contacts at the anode and cathode enables the highest device performances to be achieved.[2] For the majority of donor materials used in OPVs, PEDOT:PSS has been found to possess a sufficiently high work function to meet this requirement.[13] This factor is exemplified through recent reports of optimized thieno[3,4-b]-thiophene/benzothiophene/benzothiophene:[6,6]-phenyl C$_{71}$ butyric acid methyl ester (PTB7:PC$_{71}$BM) bulk heterojunction OPVs that exhibited certified photoconversion efficiencies exceeding 8.3% based on this anode configuration.[14]

Despite the promising electrical characteristics of OPVs that use PEDOT:PSS, its high acidity and hygroscopicity have also now been associated with long term device instability.[8,15,16] These factors cooperatively act to degrade the metallic cathodes[17] and de-dope the polymer layer itself.[18] Finding a material with the necessary electronic properties to replace PEDOT:PSS is thus a current challenge that needs to be resolved.

Transition metal oxides are a class of material that offers the necessary tunability in their electronic properties and intrinsic stability towards oxidation to be considered highly attractive for organic electronic applications.[19] The use of high work function transition metal oxides for anode modifications was first reported by Tokito et al.,[20] who demonstrated that the operating voltages of OLEDs were significantly reduced through the use of evaporated MO$_x$ (where M = vanadium, molybdenum, or ruthenium and x is the oxygen stoichiometry) layers as ITO

Dr. J. J. Jasieniak, J. Seifter, Dr. J. Jo, Prof. A. J. Heeger
Center for Polymer and Organic Solids
University of California
Santa Barbara, CA, 93106, USA
E-mail: ajhe@physics.ucsb.edu
Dr. J. J. Jasieniak
CSIRO Materials Science and Engineering
Clayton, Victoria, 3168, Australia
Dr. T. Mates
Materials Research Laboratory
University of California
Santa Barbara, CA, 93106, USA

Materials
Views
www.MaterialsViews.com

ADVANCED
FUNCTIONAL
MATERIALS
www.afm-journal.de

modifiers. Numerous groups have since reported on the incorporation of hole selective anode transition metal oxide contacts such as MoO_3,[21–24] WO_3,[25,26] V_2O_3,[24,27–29] and NiO[30,31] as suitable PEDOT:PSS replacements in OPVs and OLEDs. The general consensus from these studies is that provided the work function is adequately high, such metal oxides can provide comparable and at times superior device characteristics compared to PEDOT:PSS modified anodes, with significantly improved electrical stability. Notably, the high dielectric constant of metal oxides can also permit more favorable optical coupling to the organic layers. This effect has been recently exemplified for solar cells by Sun and co-workers who used poly(N-9″-hepta-decanyl-2,7-carbazole-alt- 5,5-(4′,7′-di-2-thienyl-3′,2′,1′-benzothiadiazole)) (PCDTBT):PC$_{71}$BM BHJ architectures to show an enhanced photocurrent for devices that used MoO_x anode modified layer instead of PEDOT:PSS.[21]

Of the above metal oxides, one of most promising candidate to emerge is MoO_3. When evaporated, this transition metal oxide possesses a Fermi level (E_F) that is pinned at 6.86 eV, an electron affinity (EA) of 6.70 eV, and an ionization energy of 9.68 eV.[32] These characteristics indicate that it is an n-type material with one of the highest EAs of any wide bandgap metal oxide semiconductor. Its high EA enables the highest occupied molecular orbital (HOMO) of many organic semiconductors to possess a sufficient density of states overlap with the empty MoO_3 conduction band states to permit for their p-type doping.[32] More recently, it has been shown that C$_{60}$, which has an ionization energy of 6.1 eV, can also undergo ground state charge transfer to MoO_3, rendering it p-doped.[33] Because of its n-type characteristics, when MoO_3 is used as a buffer layer in a solar cell configuration, the local electron depletion of the donor and acceptor phases at the interface would in principle act to reduce back-contact recombination of the electrons from fullerene acceptors, while improving hole collection from the donor materials at this interface.[34] Such a situation, may explain why evaporated MoO_3 (eMoO_3) modified anodes have been so successful in OPVs.[21,24]

For transition metal oxides, such as MoO_3, to be considered as viable PEDOT:PSS replacements in organic electronic devices, synthetic protocols which are solution processable, reproducible, harness easily accessible chemistries, and provide the necessary electrical and morphological properties must first be developed. To date, three routes that meet the majority of these requirements have been reported for the development of MoO_3 modified ITO layers.[35–37] The first utilized an acidified aqueous dispersion of ammonium molybdate that was spin coated onto ITO and heat treated at 160 °C.[35] The resulting modified surfaces exhibited 10–100 nm scale aggregates of nanocrystalline MoO_3. Solar cell devices fabricated using poly(3-hexylthiophene):[6,6]-phenyl C$_{61}$ butyric acid methyl ester (P3HT:PC$_{61}$BM) BHJs with such modified anodes exhibited comparable device characteristics to PEDOT:PSS, however, the uncontrolled and largely unfavorable surface morphology was found to reduce the shunt resistance for denser MoO_3 layers. The second route employed polymer stabilized MoO_3 nanoparticle dispersed in xylene.[36] The nanoparticle thin-films required oxygen plasma treatment to remove the polymer stabilizers and were annealed in nitrogen at 200 °C. The electronic characteristics of the resulting nanocrystalline MoO_3 layers were found

to be comparable to evaporated MoO_3 that was exposed to air. P3HT:PC$_{61}$BM BHJ solar cells fabricated using such nanoparticle modified anode also exhibited similar device characteristics to the analogous PEDOT:PSS reference devices.[22] The third route involved dissolving MoO_3 in hydrogen peroxide, which was then diluted with polyethylene glycol and 2-methoxyethanol.[37] Unlike the other two methods, the deposited thin films exhibited extremely smooth surface topographies (<0.4 nm root mean square roughness), however they required annealing temperatures of 275 °C to provide the sufficient electronic properties to be conducive to P3HT:PC$_{61}$BM BHJ devices.

In this work, we present a novel synthetic route for the development of solution-processed MoO_x (sMoO_x) anode buffer layers that is based on oxomolydate precursors. The diverse chemistry of molybdenum has enabled the development of oxometalate assemblies with significant versatility in their compositional range and structural motifs.[38,39] Here we focus on exploiting $MoO_2(acac)_2$ (acac = bis(2,4-pentanedionate)) as a precursor for the development of oxomolybdate precursor solutions. This readily available complex has been shown to undergo rapid hydrolysis in hydrated methanol solutions and condense to form dinuclear oxo-molybdate species of structural form $Mo_2O_5(OH)_2(H_2O)_4$.[40] In the limiting case of complete condensation and deprotonation, these species can result in the formation of the $[Mo_6O_{19}]^{2-}$ clusters.[40] This narrow variety of possible oxomolybdates species, suggests that this simple system presents an ideal template from which to develop controlled molybdenum oxide thin films.

The development of metal oxide thin films from such precursors and their application for organic electronics has to date not been carried out. For this reason, we undertake a detailed study to understand the evolution of their structural, chemical, and electronic properties, with the final goal being their use as anode modification layers useful in organic electronics.

2. Results and Discussions

It is well known from sol-gel chemistry that hydrolysis of precursors is required to drive the formation of metal oxides. However, for the application of such metal oxides in organic electronics, excess water content has been associated with long term instability. With this in mind, we have investigated the development of both i) anhydrous and ii) ambient synthetic routes to forming molybdenum metal oxides thin films. The anhydrous method consisted of simply heating $MoO_2(acac)_2$ directly in anhydrous methanol (<0.002% water content) within a nitrogen filled glovebox. In this manner, excessive hydrolysis from atmospheric moisture could be minimized. For the ambient method the precursor solutions were prepared in reagent grade methanol (<0.1% water content) under an ambient atmosphere. In both cases, the solutions were aged for a minimum of 2 days prior to use.

2.1. Electrospray Ionization of sMoO_x Precursor Solutions

To attain a glimpse of the molecular constituents that exist in our precursor solutions, we have employed electrospray

**ADVANCED
FUNCTIONAL
MATERIALS**

www.afm-journal.de

**Materials
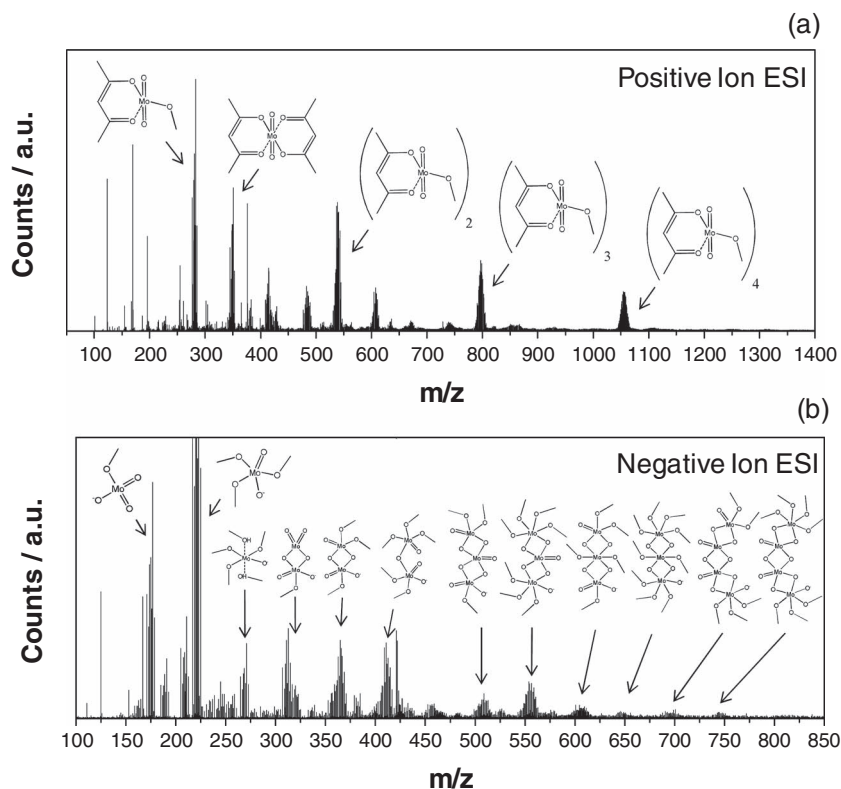Views**

www.MaterialsViews.com

Figure 1. Positive (a) and negative (b) electrospray ionization mass spectra of a dilute oxomolybdate precursor solution prepared under the ambient synthetic route. Tentative assignments of the corresponding chemical structures are depicted. All species observed in the positive ESI are associated with sodium ions. In the case of negative ESI, uncertainty in the assignments above a mass-to-charge ratio of 600 exists due to poor signal-to-noise.

ionization (ESI) mass spectroscopy. By nature of the required air exposure for this experiment, this was only performed on ambient precursor solutions. The lack of significant hydrolysis in the anhydrous route would suggest that $MoO_2(acac)_2$ complexes and potentially dinuclear clusters (e.g., $Mo_2O_5(acac)_2$) should be the dominant components. In the following sections we will show that in fact the latter species is the more likely.

In **Figure 1** we present the mass/charge spectra of the prepared oxomolybdate solutions characterized with positive (Figure 1a) and negative (Figure 1b) ESI. For clarity, the identified chemical structures of only the major mass constituents are included, with the full assignments provided in the Supporting Information (S1). In the positive ion ESI, we only observe mass contributions that arise from the starting molybdenum complex, as well as its methoxide derivative. Both of these molybdenum complexes are found to be associated with sodium ions, which are inherently observed due to residual sodium in the gas chamber. The mere fact that we only observe mononuclear complexes and their clustered analogues suggests that either these are the only species that exist in solution or they are the only species formed during the ESI process that selectively associate with the sodium.

A differing picture of our oxo-molybdate solution emerges when we compare these results to those obtained through negative ion ESI. As we are dealing with metal oxide constituents, it is more likely that we will observe more native mass spectra in

this mode as compared to positive ion, which would rely on the cleaving of the Mo–O bond (bond enthalpy ΔH^0(Mo–O) ≈ 480–670 kJ mol^{-1})[41] or sodium association. In this case, we observe an ensemble of oxo-molybdanate species, which range from mononuclear to tetranuclear, each stabilized by methoxide ligands. This result has to be treated with care as the large electric fields employed in ESI can in principle cause methoxylation of oxomolybdates or fragmentation of such species to smaller constituents.[42] For this reason, we can at best say that in our ambient precursor solutions a variety of mono- and polyoxomolybdate species exist in the native state.

2.2. FTIR Analysis of sMoO$_x$

In order to understand the chemical evolution of our anhydrous and ambient based precursors into MoO$_x$ thin films, we have performed grazing angle attenuated total reflection Fourier transform infrared spectroscopy (GA-ATR FTIR) measurements on thin films deposited on silicon as a function of thermal annealing temperature. These results are shown in **Figure 2**a,b.

Thin films deposited using the anhydrous synthetic route, then annealed at 50 °C and 100 °C, exhibit the characteristic signatures of metal acetylacetonate complexes at 1577 cm^{-1} (C=O stretch), 1530 cm^{-1} (C=C stretch), 1445 cm^{-1} (C=C stretch + C–H bend), 1420 cm^{-1} (CH$_3$ asymmetric bending), 1355 cm^{-1} (CH$_3$ symmetric bending), 1283 cm^{-1} (C–CH$_3$ stretch + C=O stretch), 1188 cm^{-1} (C–H bend), 1031 cm^{-1} (CH$_3$ rocking), and 1020 cm^{-1} (CH$_3$ rocking).[43–45] The observation of acac in the films is consistent with its strong metal chelation ability and the lack of hydrolysis in the solution. Annealing of the samples to temperatures of 200 °C causes a decrease in the contribution of all bands. Complete removal of the organics is achieved by 250 °C.

Analysis of the lower wavenumber region permits insight into the chemical nature of the Mo metal centers. At a temperature of 50 °C the existence of a split band at 940 cm^{-1} and 904 cm^{-1} is observed. This spectral region is characteristic of Mo=O bonds, and the split band indicates the existence of *cis* Mo=O bonding.[46] While mononuclear oxomolybdate species only display Mo=O and Mo–O (400–600 cm^{-1}) bonding types, polyoxomolybdates possess Mo–O–Mo bonding and thus should display stretches in the 900–500 cm^{-1} spectral region.[47] The broad band centered at 780 cm^{-1} is suggestive that such species may exist in the films at low temperatures; however, as this spectral region also corresponds to the out-of-plane bending of C–H, it cannot be unambiguously assigned.[43] At 150 °C a new band emerges at 974 cm^{-1}. Its spectral location and the concordant reduction in the cis M=O bonding are consistent with the formation of polyoxomolybdates at this temperature.[47,48] Also at this temperature, we observed a noticeable contribution to this band from an
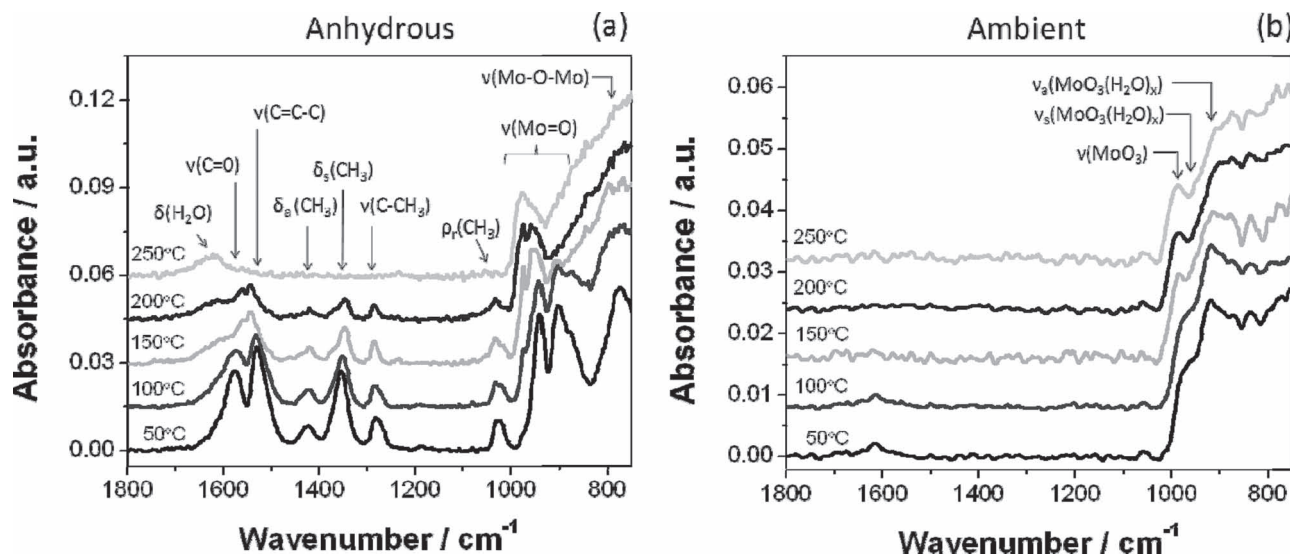
Materials
Views

www.MaterialsViews.com

ADVANCED
FUNCTIONAL
MATERIALS
www.afm-journal.de

FULL PAPER

Figure 2. GA-ATR FTIR spectra of oxomolybdate thin films deposited using a) anhydrous and b) ambient synthetic routes at varying thermal annealing temperatures in nitrogen. The assignments of the major vibrational bands are included. Underlying contributions from less dominant vibrations are omitted for clarity, but are described within the main text.

emerging shoulder at 985 cm^{-1}. This shoulder can be assigned to the stretching of terminal M=O bonds originating for a molybdenum oxide phase.[48,49] The broad band that is observed at wavenumbers below 930 cm^{-1} is believed to arise from the distorted Mo–O–Mo network that develops during its formation.[48]

For all samples studied here, we observed clear evidence of a band at 1620 cm^{-1} and a broad band centered at 3300 cm^{-1} (not shown), which correspond to the bending modes of adsorbed H$_2$O and the stretches associated with OH, respectively.[43] These contributions most likely arise from hydration of the samples due to air exposure during the FTIR measurement. Notably, the exposure of these thin-films to atmospheric moisture does gradually hydrolyse the sample, with complete hydrolysis being observed after 2 days (not shown). This time frame is the reason why ambient samples were allowed to age for a minimum of two days.

The FTIR of thin films prepared using ambient synthetic routes present a vastly different chemical landscape. Firstly, the samples exhibit undetectable quantities of residual carbon content at all temperatures. This indicates that the results obtained from positive ion ESI are indeed misleading, with the hydrolysis of the MoO$_2$(acac)$_2$ in solution sufficing to remove the acac stabilizers. Secondly, as there is no evidence of *cis* Mo=O bonding, it suggests that condensation has occured. Consistent with these observations, the broad shoulder centred at 970 cm^{-1} agrees well with the stretching frequency observed for terminal M=O bonds present in molybdic acid ((MoO$_3$(H$_2$O)$_x$)$_n$, where n and x denotes the repeating unit and level of hydration, respectively).[48] This indicates that such species likely consitute our thin films. Annealing at temperatures above 100 °C exhibits the development of a peak at 985 cm^{-1} and the concordant reduction in the water content at 1615 cm^{-1}. These observations are consistent with dehydration of the molybdic acid to form MoO$_3$ or its oxygen deficient analogue, MoO$_x$.[48]

Overall, the FTIR results show that the chemical composition of thin films made from the two synthetic routes employed here are very different. However, despite this difference, both

proceed to form molybdenum oxide phases at temperatures of 150 °C or above.

2.3. Thermogravimetric Analysis

To quantify the compositional changes as a function of temperature for both synthetic routes, we have analyzed the thermalization events of the products within our precursor solutions through thermogravimetric analysis (TGA). This data is shown in **Figure 3** for the starting material MoO$_2$(acac)$_2$ and the dried powders obtained from both anhydrous and ambient synthetic routes. TGA of the precursor material shows a dominant mass loss event with an onset of 214 °C and total loss of 39%. Assuming minimal
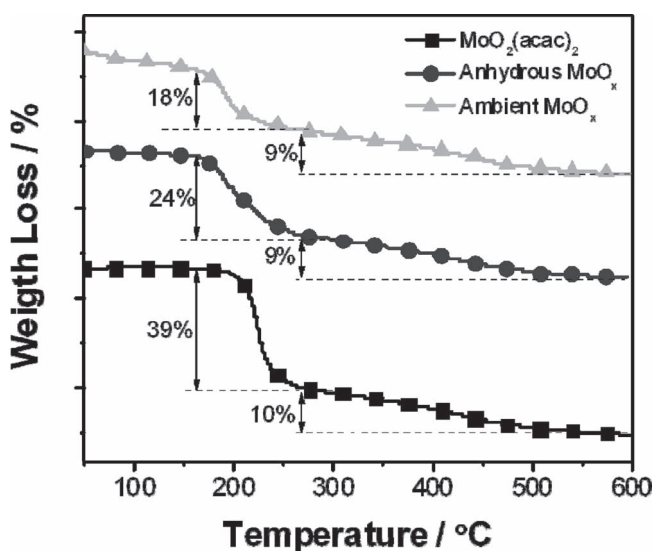

Figure 3. A comparison of the TGA of MoO$_2$(acac)$_2$ with the powders obtained from drying anhydrous and ambient MoO$_x$ precursor solutions.

Starting Material   Anhydrous Precursor   Ambient Precursor

$MoO_2(acac)_2$ $Mo_2O_5(acac)_2(MeOH)_2$ $(MoO_3)_n(H_2O)_{n+2}$ $(MoO_3)_n(H_2O)_{2n+1}$
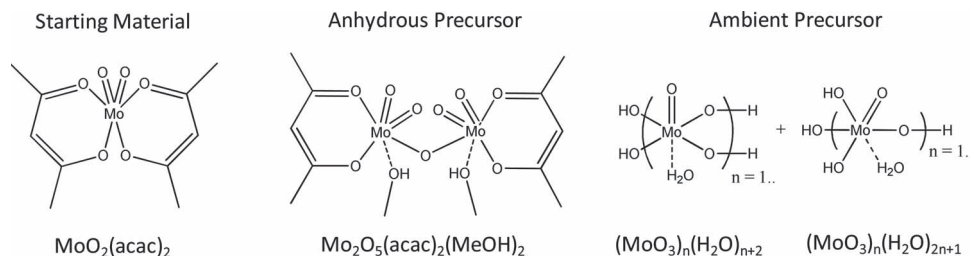
Figure 4. Chemical structures of the starting material and the precursors developed within the anhydrous and ambient synthetic routes.

hydration of the starting material, the 127 Da that this peak corresponds to cannot arise from simple acac desorption (MW_{acac} = 100 Da), but instead must accompany a decomposition event.

In comparison, the powders obtained from the anhydrous method result in a mass loss onset occurring at 190 °C and a total loss of 24%. As this mass loss event arises from acac decomposition, a comparison of its ratio to that of the starting $MoO_2(acac)_2$ suggests that these powders contain ≈60% of the acac content. This value is consistent with the formation of dinuclear species in solution, i.e., $Mo_2O_5(acac)_2(MeOH)_2$. The ambient based powders exhibit a similar thermal loss onset of 176 °C and a slightly reduced total loss of 18%. As organic contaminants are minimal in these films, the major mass loss must arise from dehydration of the identified molybdic acid phases.

It has been shown that sol-gel prepared molybdic acid phases first dehydrate to yield MoO_3, then experience oxygen loss to produce mixed $MoO_{2.5}$ and MoO_2 phases following heating under inert atmospheres to above 400 °C.[50] By considering that in our case further heating to 600 °C causes an additional 9% mass loss and assuming a similar mechanism, we can estimate the nominal composition of the molybdic acid phases in our starting materials to be approximately $MoO_3(H_2O)_{1.8}$. In **Figure 4** we present a schematic of the proposed chemical species that exist within our precursor solutions.

2.4. Surface Topography of sMoO$_x$ Thin Films

In addition to possessing the appropriate electronic structure, a desirable criterion for the employment of solution processed modifying layers in organic electronics is that their surface

structure is as smooth as possible. Atomic force microscopy (AFM) images of 10 nm thick sMoO$_x$ layers deposited on ITO were performed for both anhydrous and synthetic routes at annealing temperatures ranging between 70 °C and 250 °C (see Supporting Information S2). Each film was found to exhibit remarkably similar surface structures, with root mean square (rms) roughness values ranging between 0.3 and 0.4 nm and peak-to-trough values of ≈1 nm. Thickness dependence measurements up to 80 nm showed that these ultrasmooth film topographies were retained across this range (see Supporting Information S2). X-ray diffraction measurements showed no discernible diffraction peaks (see Supporting Information S3), indicating that the cause of this smoothness is the amorphous nature of the films.

In order to appreciate the variation in surface topography between our sMoO$_x$ and the conventionally used PEDOT:PSS anode modification layer, in **Figure 5** we show AFM images of a) bare ITO, b) ITO with a 10 nm sMoO$_x$ layer annealed at 150 °C, and c) ITO with a 40 nm PEDOT:PSS layer. The bare ITO substrate exhibits an rms roughness of 0.45 nm ± 0.06 nm, with clear evidence of grain boundaries and small surface pin-holes stemming from the commercial smoothing process. Deposition of the sMoO$_x$ onto the ITO is found to result in homogeneous film formation, which acts to fill in the existing pin-holes and remove the ITO spikes producing an rms roughness of 0.35 ± 0.06 nm. PEDOT:PSS is also found to homogenously overcoat the ITO surface, however, it does so through the formation of nanoparticle films. This factor causes the comparative surface roughness to slightly increase to 1.12 nm.

Generally, all of these rms values are adequately smooth for the incorporation into organic electronic devices. In

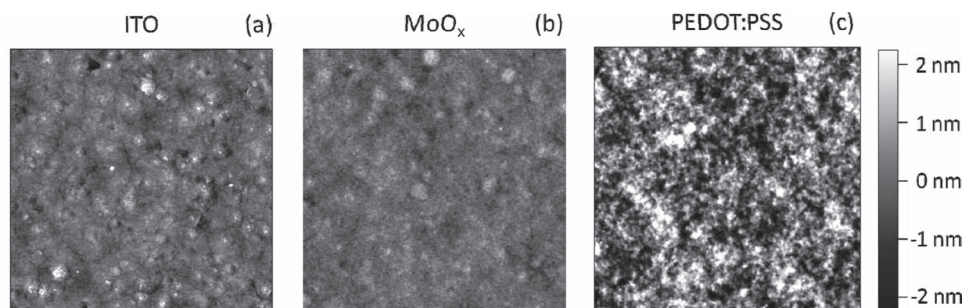ITO   (a)   MoO$_x$ (b)   PEDOT:PSS   (c)

Figure 5. AFM images showing the topological morphology of a) bare ITO, b) ITO with a 10 nm thick sMoO$_x$ thin film, and c) ITO with a 40 nm thick PEDOT:PSS layer. The corresponding rms surface roughnesses of each film, across the 2 μm × 2 μm areas shown here, are calculated to be 0.448 nm, 0.354 nm, and 1.12 nm, respectively.

www.MaterialsViews.com

ADVANCED
FUNCTIONAL
MATERIALS
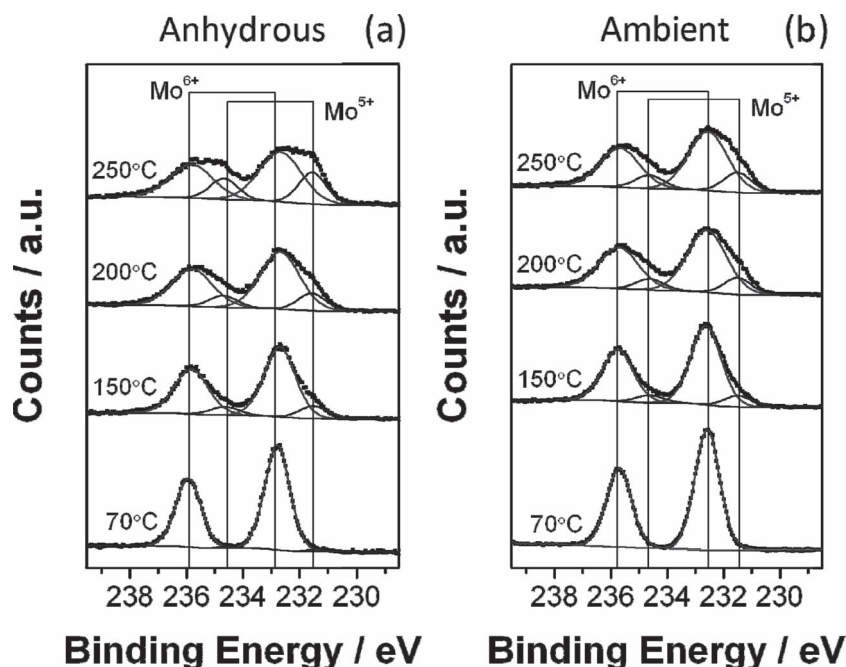www.afm-journal.de

FULL PAPER

Figure 6. High-resolution XPS data of the Mo 3d core level peaks observed for molybdenum oxide thin films prepared from a) anhydrous and b) ambient-based precursor solutions as a function of annealing temperature in a nitrogen atmosphere.

comparison, $sMoO_3$ layers made from nanoparticle suspensions possess considerably higher roughness values of between 15–30 nm.[22] These larger values arise due to the curvature of the nanoparticles and surface aggregation, two factors that are not of concern in our synthetic routes.

2.5. X-Ray Photoelectron Spectroscopy of $sMoO_x$

Having identified the chemical functionalities and structures within our solution-processed molybdenum oxide films as a function of annealing temperature, we then used X-ray photoelectron spectroscopy (XPS) to better appreciate the evolution of these chemical characteristics and to ultimately determine the Mo:O stoichiometry. In **Figure 6**a,b we show the Mo 3d core level peaks for films deposited using anhydrous and ambient synthetic routes on ITO, respectively. A summary of the peak binding energies and peak widths obtained from the analyses of these regions are included in the Supporting Information S4. Both samples exhibit similar spectral characteristics as a function of annealing temperature. At 70 °C a dominant Mo 3d doublet is observed with a 3.1 eV spin-orbit splitting between the Mo $3d_{3/2}$ and $3d_{5/2}$ bands. The peak energy of the Mo 3d band is observed at a ≈0.2 eV higher binding energy in the anhydrous sample (232.9 eV) as compared to that prepared under ambient conditions (232.7 eV). The higher binding energy of the anhydrous sample is tentatively ascribed to a reduced electronic coupling between the forming molybdenum oxide film and the ITO substrate due to the presence of stabilizing organic groups. Despite this minor difference, the magnitude of the binding energies is consistent with the reported values of Mo^{6+} species existing in a variety of molybdenum oxide clusters as well as

crystalline MoO_3.[51,52] At higher annealing temperatures, a secondary contribution to the Mo 3d doublet is also observed to grow at ≈1.1 eV lower binding energies. This contribution is consistent with the formation of Mo^{5+} species, and concomitant with the presence of oxygen deficiencies.[52]

The nature of the peak broadening gives an indication of the molybdenum coordination that exists. Mo^{6+} that is located within octahedral environments has been found to exhibit a peak broadening of ≈1.0 eV, while that incorporated in non-octahedral environments exhibited an increased broadening to 1.55 eV.[53] The ≈1.05 eV Mo 3d peak broadening that is observed at 70 °C for both preparation routes is consistent with an octahedral coordination of the molybdenum metal centers. Higher temperatures exhibit a gradual increase in the peak broadening, suggesting the distortion of this coordination. As the broadening is concordant with the formation of the reduced Mo^{5+} species, it suggests that the gradual dehydration and thermalization of the organics that occur at the elevated temperatures are a cause of this distortion in the molybdenum oxide films.

FTIR analysis of metal oxide films prepared under anhydrous conditions showed that significant acac stabilization remains in the film at temperatures below 200 °C. This raises the question of whether we are predominantly depositing thin films of our starting material, $MoO_2(acac)$. XPS of neat $MoO_2(acac)_2$ exhibits a Mo $3d_{5/2}$ peak energy that is ≈0.7 eV lower than that of MoO_3.[54] This arises because the low electronegativity of the acac (2.4) compared to oxygen (3.44) ensures that a comparatively higher electron density is located on the Mo^{6+} center in the complex. The observed 232.7–232.9 eV binding energies of the Mo $3d_{5/2}$ for our anhydrous samples confirm that the original complexes are modified in solution, likely to the proposed dinuclear species.

To compliment the FTIR analysis, and to approximate the Mo:O stoichiometry of the various films, in **Table 1** we provide a summary of the compositional analysis obtained from XPS survey spectra (see Supporting Information S5). Consistent with the thermalization of the organic stabilizers observed from infrared analysis, the carbon content in the anhydrous synthetic route is found to decrease drastically with increasing annealing temperature. By nature of the hydrolysis under ambient conditions and the consequent removal of the majority of stabilizers, the comparative carbon content for cluster solutions prepared under ambient conditions is significantly lower.

A survey of the various studies that have used molybdenum oxides as an anode modifying layer for organic electronics, suggests that a wide variation in the specific Mo:O stoichiometry can be tolerated in achieving high performance.[20–22,36,55] As the above samples were prepared on ITO, the underlying contribution of oxygen from the substrate compromises the quantitative determination of the Mo:O stoichiometry. For this reason, samples were also prepared using an ambient synthetic route on Au substrates (see Supporting Information S6).

Table 1. XPS compositional analysis of the relative oxygen, carbon and molybdenum content in the solution processed molybdenum oxide films deposited on ITO using anhydrous and ambient synthetic routes at different annealing temperatures (T_a). Included is the calculated Mo^{5+}/Mo^{6+} ratio based on the analysis of high resolution Mo 3d contributions. Using this ratio, the effective molybdenum to "lattice" oxygen ratio is thus calculated.

Sample Preparation	T_a [°C]	O 1s	C 1S	Mo 3d	Mo^{5+}/Mo^{6+}	Mo:O
Anhydrous	70	4.23	3.48	1.00	0.02	1:2.99
Anhydrous	150	4.63	2.51	1.00	0.16	1:2.93
Anhydrous	200	4.68	2.08	1.00	0.22	1:2.91
Anhydrous	250	4.54	1.64	1.00	0.41	1:2.86
Ambient	70	3.81	1.31	1.00	0.00	1:3.00
Ambient	150	3.93	1.27	1.00	0.12	1:2.95
Ambient	200	3.65	1.04	1.00	0.19	1:2.92
Ambient	250	3.68	1.04	1.00	0.25	1:2.90

The analysis of these samples validates that for systems which only possessed Mo^{5+} and/or Mo^{6+} species, the minimum Mo:O stoichiometry can be estimated directly from the known Mo^{5+}/Mo^{6+} ratio (see Supporting Information S7). By using the Mo^{5+}/Mo^{6+} obtained from the high-resolution core level spectra above, the Mo:O stoichiometries of the samples made on ITO at the various annealing temperatures were thus determined (see Table 1). The samples exhibit a nearly ideal MoO_3 lattice stoichiometry at low annealing temperatures. At higher temperatures the films become progressively more deficient in oxygen, approaching compositional values of $MoO_{2.85}$ at 250 °C.

2.6. Ultraviolet Photoelectron Spectroscopy of sMoO$_x$

In vacancy-free oxomolybdate clusters, the valence band is determined by O 2sp molecular orbitals. The development of oxygen deficiencies introduces reduced Mo 4d species which define sub-gap states that emerge at binding energies higher than ≈0.4 eV with respect to the Fermi level.[51] As is well known from bulk semiconductor interfaces, sub-gap states act to alter the charge distribution at the interface, thus giving rise to the possibility of surface-state pinning in heterojunctions.[34] The role of MoO_x sub-gap states in defining the interfacial electronic properties with semiconducting organic layers has been explored by Kanai et al.[56] The authors showed that charge transfer between the organic hole transporting molecule N,N'-di(naphthalene-1-yl)-N,N'-diphenyl-benzidinie (α-NPD) and the reduced Mo 4d states act to pin the HOMO level of the NPD. This observation suggests that the charge transport properties across these junctions would be defined by these Mo 5+ defect states, as opposed to the valance or conduction band edges. For the application of MoO_x films in organic electronics, it is thus vital to identify the existence of such states and further elucidate their involvement in the interfacial charge transport properties. To this extent, we have investigated the electronic structure of our $sMoO_x$ films using ultraviolet photoelectron spectroscopy (UPS) deposited through the anhydrous and ambient synthetic routes as a function of annealing temperature.
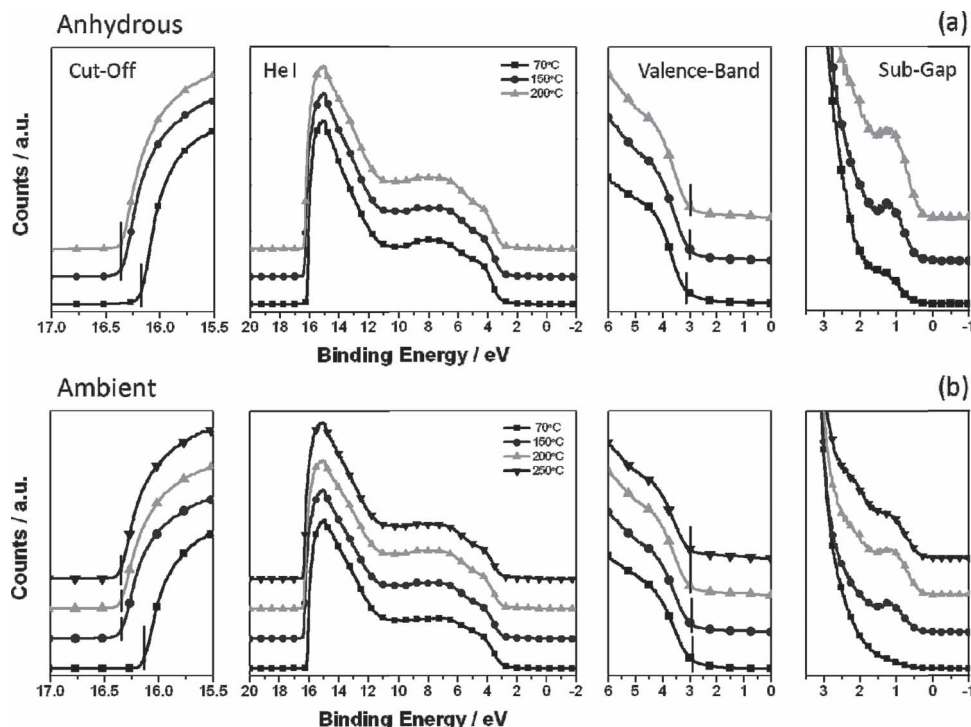
Figure 7. UPS spectra of molybdenum oxide thin films prepared from using a) anhydrous and b) ambient synthetic routes as a function of annealing temperature in a nitrogen atmosphere. The full UPS spectrum using He I radiation (center), secondary-electron cutoff (left), the valence-band region (right) and the magnified (≈10×) sub-gap region (far right) are included. Due to charging of the 250 °C sample prepared using the anhydrous route, the UPS spectrum could not be obtained.

Materials
Views
www.MaterialsViews.com

ADVANCED
FUNCTIONAL
MATERIALS
www.afm-journal.de

FULL PAPER

Table 2. Summary of the energy level landscape determined from UPS (He I) and optical absorption spectra for the solution processed MoO_x ($sMoO_x$) using anhydrous and ambient synthetic routes at varying annealing temperatures (T_a). Samples were measured on ITO, for which the work function was measured to be 4.3 eV. A comparison to literature values of evaporated MoO_3 ($eMoO_3$) and ozone treated MoO_3 nanoparticles (NP) is also included.[32,33,36] The notations in the table E_g, E_F, IE, IE_{GS}, and EA, denote the electronic band-gap, Fermi-energy (vs. vacuum), valence band ionization energy, sub-gap state ionization energy, and electron affinity, respectively.

MoO_x Sample	T_a [°C]	E_g [eV]	E_F [eV]	IE [eV]	IE_{GS} [eV]	EA [eV]
Anhydrous $sMoO_x$	70	3.3	5.0	8.2	5.5	4.9
Anhydrous $sMoO_x$	150	3.2	4.9	7.9	5.4	4.7
Anhydrous $sMoO_x$	200	3.2	4.9	7.9	5.3	4.7
Ambient $sMoO_x$	70	3.3	5.1	8.0	N/A	4.7
Ambient $sMoO_x$	150	3.2	4.9	7.9	5.4	4.7
Ambient $sMoO_x$	200	3.1	4.9	7.9	5.3	4.8
Ambient $sMoO_x$	250	3.1	4.9	7.9	5.3	4.8
$eMoO_3$	RT	3.2	6.9	9.8	N/A	6.6
$eMoO_3$ air-exposed	RT	3.2	4.9	7.9	N/A	4.7
NP $sMoO_3$ ozone-treated	RT	3.2	5.4	8.3	N/A	5.1

The UPS spectra of our $sMoO_x$ films are shown in **Figure 7**. Magnified regions of the photoemission cut-off, valence band and sub-gap states are included. The valence band ionization energies (IE), Fermi levels (E_F), and sub-gap state ionization (IE_{GS}) calculated from each of these respective regions are summarized in **Table 2**. For completeness, the optical bandgaps (E_g) of the thermally evolving metal oxide films deposited on quartz were measured using absorption spectroscopy (see Supporting Information S8). The E_g ranged between 3.1 and 3.3 eV; these values are consistent with oxomolybdate clusters and MoO_3.[32] As the optical bandgap is equal to or greater than the electrical bandgap in inorganic semiconductors, the electron affinities (EA) could be estimated from the IE values.

The photoemission cut-off and valence-band onset energies show that E_F and IE for both synthetic routes experience a slight decrease above 70 °C, at which point they stabilize to a value of 4.9 eV and 7.9 eV, respectively. The trend in the EA values show an opposing, albeit slight, variation, with the values stabilizing at 4.7 eV and 4.8 eV for the anhydrous and ambient routes, respectively. Overall, the mapped out electronic landscapes that the above analysis presents indicate that, despite the chemical difference, all the metal oxide films possess similar electronic structures and are n-doped.

The intrinsic mechanism for n-doping in binary metal oxide systems is for oxygen deficiencies to exist within the film. The reduced Mo 4d states that such deficiencies create are evidenced in the magnified region close to the valence band edge (see Figure 7). These sub-gap states are found to emerge at binding energies of ≈0.4–0.5 eV above the MoO_x Fermi level and increase in magnitude with increasing annealing temperature. For the MoO_x sample prepared under ambient conditions and annealed at only 70 °C, this contribution is not resolved. This is unlike the anhydrous preparation, where a minor development

of these states is observed. These observations are in agreement with the XPS results, which show the emergence of Mo^{5+} contributions to the Mo 3d core level peaks only for the anhydrous preparation at this temperature. Indeed, the increase in the magnitude of these sub-gap states is also correlated to the increased quantity of the Mo^{5+} species observed in XPS.

The work function of $eMoO_3$ is highly sensitive to oxygen, moisture and organic adsorbates.[57,58] Gradual exposure to such elements have been shown to result in a drastic shift of the $eMoO_3$ energy levels towards the vacuum level (see Table 2). By nature of the solution deposition process, $sMoO_x$ layers are expected to be contaminated in a similar way. The comparable electronic structure of our thin films at annealing temperatures of 150 °C and above to that of air exposed $eMoO_3$ confirms this assumption. Notably, similar values have also been found for $sMoO_3$ nanoparticle layers,[36] which have been successfully used as anode modifying layers in BHJ solar cells.[22]

2.7. $sMoO_x$ Modified Anodes for P3HT:PC_{61}BM OPVs

The interfacial and electronic properties of metal oxide based modifying layers for organic electronic devices can have drastic influences on their resulting performance. The $sMoO_x$ deposited here using both synthetic routes present vastly different chemistries, but yet similar electronic characteristics. To investigate the influence of these variations within OPVs, we have utilized the archetypal P3HT:PC_{61}BM BHJ system as a test case.

In **Figure 8** we present the current-voltage (J–V) curves of OPVs fabricated using 10 nm anhydrous (Figure 8a,b) and ambient (Figure 8c,d) based $sMoO_x$ modified anodes as a function of metal oxide annealing temperature. This thickness was found to be within the optimal range (10–20 nm) for achieving the highest device performance (see Supporting Information S9). All devices were thermally annealed at 150 °C for 10 min following the aluminium cathode evaporation to induce appropriate re-crystallization of the BHJ.[59] The extrapolated device parameters of these OPVs are summarized in **Table 3**.

Despite the significant difference in the chemistries presented through both synthetic routes, the devices exhibit similar trends in performance at all comparative annealing temperatures. Using an annealing temperature of 70 °C, devices with short circuit current density, J_{sc} of ≈9.5 mA cm^{-2}, fill factors (FF) approaching 70%, open circuit voltage, V_{oc}, of 0.59 V and power conversion efficiencies (PCE) of above 3.5% were achieved. These efficiencies are directly comparable to analogous devices fabricated using the conventionally used PEDOT:PSS as an anode modifying layer (see Supporting Information S10,11). Advantageously, while both $sMoO_x$ and PEDOT:PSS based P3HT:PCBM solar cell devices exhibited comparable efficiencies, exposure to ambient conditions revealed that the $sMoO_x$-based devices exhibited a greater than sixfold increase in their efficiency half-life (see Supporting Information S12). This enhancement is an indication of the more stable nature of the $sMoO_x$-modified anodes that form, and its more favorable affect on the aluminium cathode and/or BHJ active layer stability.

While $sMoO_x$ originally annealed at 70 °C was found to be amicable to the development of high efficiency P3HT:PCBM solar cells, a gradual increase of the annealing temperature
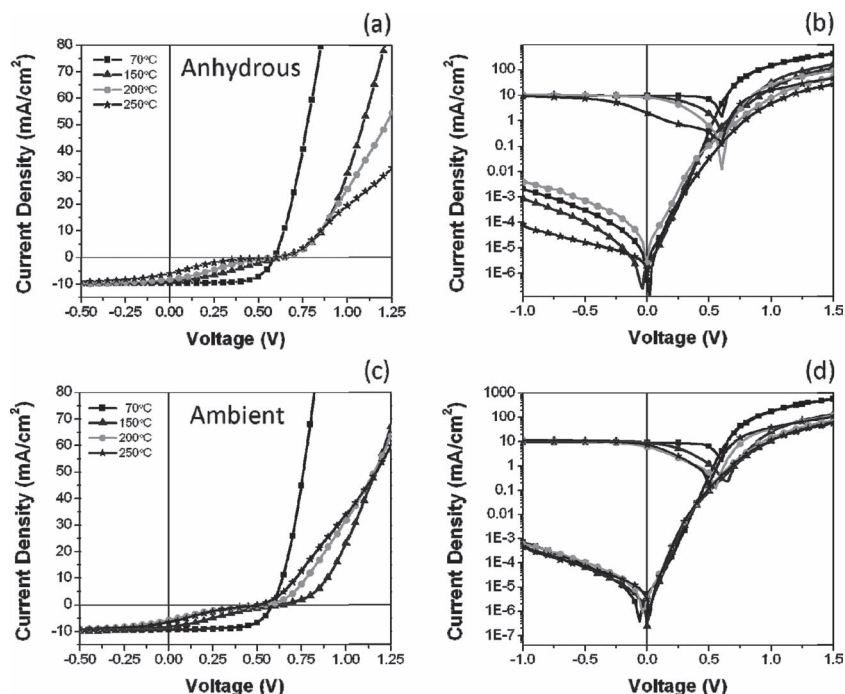
FULL PAPER

Figure 8. *J*–*V* characteristics of P3HT:PC$_{61}$BM solar cells fabricated with an anhydrous (a,b) and ambient (c,d) based, 10 nm thick, sMoO$_x$ anode modifying layer annealed at different temperatures.

treated at different temperatures were carried out (see Supporting Information S13). It was found that the relative evolution of Mo^{5+} states is suppressed by the presence of the BHJ film. This causes the density of these states within the sMoO$_x$ to be significantly lower for the film initially annealed at 70 °C compared to 150 °C, even though both were subsequently annealed at 150 °C in the presence of the BHJ film. The fundamental difference that this presents hints that the origin of the above device performance trends is directly associated with the density of the Mo^{5+} species within the sMoO$_x$.

S-shape features of the *J*–*V* curves under light with a concurrent reduction of dark currents in OPVs have been primarily related to the accumulation of charges by resistive layers[60,61] or to the formation of dipoles[62] at the anode or cathode. In OPVs that incorporate metal oxide buffer layers, s-shape characteristics are commonly observed when only light below the bandgap of the oxide is incident.[63] Upon illumination with a broad spectrum these effects vanish. This improvement can be considered as arising from the enhanced conductivity of the metal oxide films under light due to trap filling[64] or photodoping.[65] In both cases, the enhanced conductivity of the metal oxides would prevent accumulation of charges at the metal oxide interface. Resistivity measurements for our sMoO$_x$ films show that increasing temperature from 70 °C to 250 °C decreases the resistivity from >100 MΩ cm to ≈70 kΩ cm, respectively (see Supporting Information S14). This opposing trend compared to the observed *J*–*V* characteristics, indicates that the limited sMoO$_x$ conductivity is not a concern.

The s-shape character must therefore arise due to an interfacial resistance or unfavourable dipole. An increased interfacial resistance can be envisaged if either an extraction or injection barrier exist,[60] unfavorable vertical phase separation is present[66] or a chemical reaction between either of the BHJ constituents and the sMoO$_x$ has taken place. On the other hand, an unfavorable interfacial dipole may arise from molecular arrangement, induced defects, or traps.[62] The existence of Mo^{5+} sub-gap states in the sMoO$_x$, and their increasing density at higher annealing temperatures, correlate to more prominent s-shape characteristics within our P3HT:PC$_{61}$BM devices. However, the presence of such gap states may contribute to either of the above interfacial phenomena. A deeper understanding of this problem is required, but is outside the scope of the present work. To address this, a detailed study of the subtle nature of this interface with P3HT:PC$_{61}$BM, as well as other donor:acceptor systems, is currently under way.

resulted in the devices exhibiting an s-shape character to their *J*–*V* curves and thus becoming progressively worse. This behavior was accompanied by a gradual increase of the series resistance, resulting in a greater than fourfold decrease of the dark injection current at equivalent large positive biases when comparing sMoO$_x$ annealed at 70 °C to that annealed at 150 °C and above.

By nature of the post-production thermal annealing protocol employed here, all the samples were annealed at 150 °C post cathode deposition. Despite this factor, the devices fabricated with sMoO$_x$ at 70 °C were better than those annealed at 150 °C. To investigate whether the origin of this anomalous behavior stemmed from the sMoO$_x$, XPS measurements of thin P3HT:PC$_{61}$BM films annealed at 150 °C on sMoO$_x$ thermally

Table 3. A summary of the device characteristics obtained for P3HT/PC$_{61}$BM solar cells fabricated using a 10 nm thick sMoO$_x$ layer that was annealed at various temperatures. Series resistance (R_S) values were measured at 1.5 V. For completeness, we also include the shunt resistance (R_{Shunt}) values for each of the devices.

Route	T_a [°C]	R_S [Ω cm^2]	R_{Shunt} [MΩ cm^2]	J_{SC} [mA cm^{-2}]	V_{OC} [V]	FF [%]	PCE [%]
Anhydrous	70	1.6	31	9.5	0.59	68	3.8
Anhydrous	150	3.6	58	8.8	0.62	47	1.7
Anhydrous	200	7.8	7.8	8.3	0.60	22	1.1
Anhydrous	250	15	41	2.0	0.58	18	0.22
Ambient	70	1.1	52	9.2	0.59	66	3.6
Ambient	150	7.1	21	7.6	0.64	19	1.4
Ambient	200	6.7	15	6.3	0.56	16	0.57
Ambient	250	7.9	15	6.6	0.51	18	0.61

3. Conclusions

In this work we have developed two methanol based protocols which permit the formation of oxomolybdate precursors under

www.MaterialsViews.com

ADVANCED
FUNCTIONAL
MATERIALS
www.afm-journal.de

FULL PAPER

anhydrous and hydrated conditions. These precursor solutions enable the deposition of ultrasmooth MoO_x thin films, with the appropriate electronic and structural properties to be conducive in organic electronics. To exemplify this, bulk heterojunction solar cells based on P3HT:PC_{61}BM active layers utilizing such MoO_x-modified anodes have been studied. The device performance was found to depend strongly on the density of Mo^{5+} species within the sMoO_x. Only when the density of such states was minimized, solar cells with performances comparable to PEDOT:PSS modified anodes could be achieved. Overall, the simple oxomolybdate precursors that we have developed are a viable candidate for replacing the PEDOT:PSS anode modifying layers in many organic solar cells, as well as other electronic devices, that require an ultrasmooth solution-processed hole selective contact.

4. Experimental Section

MoO_x Precursor Solution Preparation and Characterization: MoO_x precursor solutions were prepared using an anhydrous and an ambient synthetic route. For the anhydrous route, Molybdenum (VI) oxide bis(2,4-pentanedionate) (MoO_2(acac)$_2$, Alfa Aesar, 99%) was heated directly in anhydrous methanol (Aldrich) for 2 h at 60 °C in nitrogen filled glovebox (O_2 content <50 ppm, H_2O content <10 ppm). For the ambient route, the precursor solutions were analogously prepared with the exception that reagent grade methanol (Fischer Scientific) was used and heating was performed in air. Both solutions were cooled to room temperature and aged for 2 days prior to use. The film thicknesses measured by AFM of sMoO_x when spin coated onto UV-ozone treated ITO at 3000 rpm for 30 s with varying MoO_2(acac)$_2$ concentrations in methanol were: 10 nm at 23 mM (7.5 mg mL^{-1}), 20nm at 46 mM (15 mg mL^{-1}), 40 nm at 92 mM (30 mg mL^{-1}), and 80 nm at 184 mM (60 mg mL^{-1}). These solutions were prepared by dilution from a filtered (0.2 μm polytetrafluoroethylene (PTFE) filter) stock 184 mM.

ESI: Electrospray ionization mass spectroscopy was performed on a Waters micromass QTOF2 mass spectrometer with an electrospray ionization source. The MoO_x precursor solutions were introduced via direct infusion from a Harvard Apparatus Syringe Pump at a rate of 5 μL min^{-1}. Source and desolvation temperatures were set at 80 °C and 100 °C, respectively. The electrospray capillary voltage was held at 3.5 kV in positive ion mode and 2.0 kV in negative ion mode. The skimmer cone voltage was held between 10 and 45 V. Altering the cone voltage did not appear to affect the distribution of the observed mass peaks. Spectral analysis was carried out using MassLynx V4.1.

FTIR: FTIR spectroscopy was performed on a Nicolet Magna 850 FTIR Spectrometer with Harrick GA-ATR attachment operating at a fixed incident angle of 65°. sMoO_x thin films, of thickness 40–80 nm, were deposited on a silicon wafer with a native silicon oxide. The obtained infrared spectra were baselined with respect to air and then, subsequently, the contribution of silicon was manually removed. Due to experimental restrictions, measurements were performed on samples after exposure to air for between 20–60 min, with samples being measured in random order to avoid error. Slight differences in observed water content between the anhydrous and ambient methods are believed to arise from variations in humidity on the day of each sample's measurement.

TGA: TGA was performed on a Mettler TGA/sDTA 851e under nitrogen flow rate of 50 mL min^{-1}. The MoO_2(acac)$_2$ was used as received. For the measurements on the precursor solutions, the samples were dried under nitrogen flow (anhydrous sample dried in the glovebox) at room temperature and placed under vacuum overnight (pressure of <1 Torr). The anhydrous sample was exposed to air for ≈5 min prior to TGA measurement.

UPS/XPS: UPS and XPS were performed using a Kratos Axis Ultra XPS/UPS system (Kratos Analytical, Manchester, UK). For XPS, survey scans to identify overall surface composition were performed using a monochromated Al k-alpha X-ray source (1486.6 eV), detecting photoelectrons at 160 eV pass energy and a channel width of 500 meV. High-resolution scans to identify bonding states were performed at 20 eV pass energy and 50 meV channel width. Repetitive test scans were run to assure that X-ray exposure was not altering the bonding state of the molybdenum. All samples were referenced to the In 3d$_{5/2}$ contribution at 445.2 eV, with an estimated error of ±0.1 eV.[67] UPS was carried out using He I radiation at 21.2 eV from a discharge lamp operated at 90 W, a pass energy of 10 eV, and a channel width of 25 meV. Conductive, grounded samples were run without charge compensation. A –9 V bias was applied to the samples in order to separate the sample and analyzer low-kinetic-energy cutoffs. As a point of reference for our UPS, measurements performed on neat ITO resulted in a work function of 4.3 eV (see Supporting Information S15). The error in the UPS measurements is at approximated as ±0.15 eV based on the width of the Fermi edge of a reference gold sample.

AFM: Tapping mode AFM was carried out in room-temperature air with an MFP-3D-SA Atomic Force Microscope made by Asylum Research. FORTA probes from Applied Nanostructures were used, which had a silicon cantilever of nominal spring constant of 3.0 N m^{-1}, a nominal resonance frequency of ≈60 kHz, and were tuned to a rms cantilever oscillation amplitude of ≈1000 mV. Acquired images of 2 μm × 2 μm were taken with a scan frequency of 1 Hz. Root mean square roughness was calculated over 2 μm × 2 μm, with the error in the measurements due to instrument noise being ±0.06 nm, as quoted by Asylum.

Photovolatic Cell Fabrication and Testing: Solar cells were fabricated on ITO-coated glass substrates that was purchased from Thin Film Devices, Inc. The ITO-coated glass substrates were first cleaned with detergent, ultrasonicated in water, acetone, and isopropyl alcohol, and UV-ozone treated for 1 h. sMoO_x films were deposited onto ITO substrates by spin coating the precursor solutions at different concentrations and spin speeds to obtain the appropriate thicknesses. Anhydrous sMoO_x films were deposited and annealed within a glovebox. Ambient sMoO_x was deposited in air and then annealed in the glovebox. PEDOT:PSS (Baytron PH) was spin coated from aqueous solution at 5000 rpm for 40 s to form a 40 nm film and dried at 150 °C in air for 10 min.

P3HT:PC_{61}BM devices were fabricated by heating separate solutions of 30 mg mL^{-1} P3HT (Konarka) and 24 mg mL^{-1} PC_{61}BM (Konarka) in chlorobenzene at 70 °C for 1 h. Upon cooling to room temperature, equimolar amounts of each solution were combined and stirred for 30 min at room temperature. Solar cells were fabricated by filtering the final P3HT:PC_{61}BM (15 mg mL^{-1}:12 mg mL^{-1}) solution through a 0.2 μm PTFE filter onto ITO, ITO/PEDOT:PSS, or ITO/sMoO_x substrates, then spin coating at 1500 rpm for 30 s.

Each device was completed by thermally evaporating aluminum cathodes (≈100 nm) through a shadow mask under a vacuum of about 8 × 10^{-6} Torr. The active area of the devices was either 19.60 mm^2 or 4.5 mm^2. During the measurement, an aperture with the area of 12.38 mm^2 was used for the 19.60 mm^2 devices. Device performances for both active areas were similar. *J–V* characteristics were measured using a Keithley 2400 Source Measure Unit. Solar cell performance used an Air Mass 1.5 Global (AM 1.5 G) solar simulator with an irradiation intensity of 100 mW cm^{-2}. Incident photon conversion efficiency (IPCE) spectra were measured by using a QE measurement system (PV measurements, Inc.). The integrated IPCE values were always within a few percent of the measured short-circuit current densities.

Supporting Information

Supporting Information is available from the Wiley Online Library or from the author.

FULL PAPER

Acknowledgements

[1] R. Steim, F. R. Kogler, C. J. Brabec, *J. Mater. Chem.* **2010**, *20*, 2499.

[2] R. H. Friend, R. W. Gymer, A. B. Holmes, J. H. Burroughes, R. N. Marks, C. Taliani, D. D. C. Bradley, D. A. D. Santos, J. L. Bredas, M. Logdlund, W. R. Salaneck, *Nature* **1999**, *397*, 121.

[3] C. W. Tang, *Appl. Phys. Lett.* **1986**, *48*, 183.

[4] J. J. M. Halls, C. A. Walsh, N. C. Greenham, E. A. Marseglia, R. H. Friend, S. C. Moratti, A. B. Holmes, *Nature* **1995**, *376*, 498.

[5] G. Yu, J. Gao, J. C. Hummelen, F. Wudl, A. J. Heeger, *Science* **1995**, *270*, 1789.

[6] C. W. Tang, S. A. Van Slyke, *Appl. Phys. Lett.* **1987**, *51*, 913.

[7] N. C. Greenham, S. C. Moratti, D. D. C. Bradley, R. H. Friend, A. B. Holmes, *Nature* **1993**, *365*, 628.

[8] F. So, D. Kondakov, *Adv. Mater.* **2010**, *22*, 3762.

[9] M. P. de Jong, L. J. van Ijzendoorn, M. J. A. de Voigt, *Appl. Phys. Lett.* **2000**, *77*, 2255.

[10] Y. Cao, G. Yu, C. Zhang, R. Menon, A. J. Heeger, *Synth. Met.* **1997**, *87*, 171.

[11] S. A. Carter, M. Angelopoulos, S. Karg, P. J. Brock, J. C. Scott, *Appl. Phys. Lett.* **1997**, *70*, 2067.

[12] T. M. Brown, J. S. Kim, R. H. Friend, F. Cacialli, R. Daik, W. J. Feast, *Appl. Phys. Lett.* **1999**, *75*, 1679.

[13] S. H. Park, A. Roy, S. Beaupre, S. Cho, N. Coates, J. S. Moon, D. Moses, M. Leclerc, K. Lee, A. J. Heeger, *Nat. Photonics* **2009**, *3*, 297.

[14] Z. He, C. Zhong, X. Huang, W.-Y. Wong, H. Wu, L. Chen, S. Su, Y. Cao, *Adv. Mater.* **2011**, *23*, 4636.

[15] K. Norrman, M. V. Madsen, S. A. Gevorgyan, F. C. Krebs, *J. Am. Chem. Soc.* **2010**, *132*, 16883.

[16] M. Jørgensen, K. Norrman, F. C. Krebs, *Sol. Energy Mater. Sol. Cells* **2008**, *92*, 686.

[17] T. Yamanari, T. Taima, J. Sakai, J. Tsukamoto, Y. Yoshida, *Jpn. J. Appl. Phys* **2010**, *49*, 01AC02.

[18] K. Kawano, R. Pacios, D. Poplavskyy, J. Nelson, D. D. C. Bradley, J. R. Durrant, *Sol. Energy Mater. Sol. Cells* **2006**, *90*, 3520.

[19] Y. Xu, M. A. A. Schoonen, *Am. Mineral.* **2000**, *85*, 543.

[20] S. Tokito, K. Noda, Y. Taga, *J. Phys. D: Appl. Phys.* **1996**, *29*, 2750.

[21] Y. Sun, C. J. Takacs, S. R. Cowan, J. H. Seo, X. Gong, A. Roy, A. J. Heeger, *Adv. Mater.* **2011**, *23*, 2226.

[22] T. Stubhan, T. Ameri, M. Salinas, J. Krantz, F. Machui, M. Halik, C. J. Brabec, *Appl. Phys. Lett.* **2011**, *98*.

[23] K. J. Reynolds, J. A. Barker, N. C. Greenham, R. H. Friend, G. L. Frey, *J. Appl. Phys.* **2002**, *92*, 7556.

[24] V. Shrotriya, G. Li, Y. Yao, C. W. Chu, Y. Yang, *Appl. Phys. Lett.* **2006**, *88*, 073508.

[25] J. Meyer, S. Hamwi, T. Bulow, H. H. Johannes, T. Riedl, W. Kowalsky, *Appl. Phys. Lett.* **2007**, *91*, 113506.

[26] C. Tao, S. P. Ruan, G. H. Xie, X. Z. Kong, L. Shen, F. X. Meng, C. X. Liu, X. D. Zhang, W. Dong, W. Y. Chen, *Appl. Phys. Lett.* **2009**, *94*, 043311.

[27] C.-P. Chen, Y.-D. Chen, S.-C. Chuang, *Adv. Mater.* **2011**, *23*, 3859.

[28] K. Zilberberg, S. Trost, H. Schmidt, T. Riedl, *Adv. Energy Mater.* **2011**, *1*, 377.

[29] K. Zilberberg, S. Trost, J. Meyer, A. Kahn, A. Behrendt, D. Lützenkirchen-Hecht, R. Frahm, T. Riedl, *Adv. Funct. Mater.* **2011**, *21*, 4776.

[30] M. D. Irwin, D. B. Buchholz, A. W. Hains, R. P. H. Chang, T. J. Marks, *Proc. Natl. Acad. Sci. USA* **2008**, *105*, 2783.

[31] K. X. Steirer, J. P. Chesin, N. E. Widjonarko, J. J. Berry, A. Miedaner, D. S. Ginley, D. C. Olson, *Org. Electron.* **2010**, *11*, 1414.

[32] M. Kröger, S. Hamwi, J. Meyer, T. Riedl, W. Kowalsky, A. Kahn, *Org. Electron.* **2009**, *10*, 932.

[33] Irfan, M. Zhang, H. Ding, C. W. Tang, Y. Gao, *Org. Electron.* **2011**, *12*, 1588.

[34] B. G. Streetman, S. Banerjee, *Solid State Electronic Devices*, 5th ed., Prentice Hall, Upper Saddle River, NJ **2000.**

[35] F. Liu, S. Shao, X. Guo, Y. Zhao, Z. Xie, *Sol. Energy Mater. Sol. Cells* **2010**, *94*, 842.

[36] J. Meyer, R. Khalandovsky, P. Görrn, A. Kahn, *Adv. Mater.* **2011**, *23*, 70.

[37] C. Girotto, E. Voroshazi, D. Cheyns, P. Heremans, B. P. Rand, *ACS Appl. Mater. Interfaces* **2011**, *3*, 3244.

[38] D. L. Long, E. Burkholder, L. Cronin, *Chem. Soc. Rev.* **2007**, *36*, 105.

[39] M. T. Pope, *Inorg. Chem.* **1972**, *11*, 1973.

[40] M. R. Pedrosa, R. Aguado, V. Díez, J. Escribano, R. Sanz, F. J. Arnáiz, *Eur. J. Inorg. Chem.* **2007**, 3952.

[41] B. d. Darwent, *Bond Dissociation Energies in Simple Molecules*, Vol. *31*, U.S. Dept. of Commerce, National Bureau of Standards, Washington, D.C. **1970.**

[42] W. Henderson, J. S. McIndoe, *Mass Spectrometry of Inorganic and Organometallic Compounds*, John Wiley & Sons Ltd., West Sussex **2005.**

[43] K. Nakamoto, *Infrared and Raman Spectra of Inorganic and Coordination Compounds*, 4th ed., John Wiley & Sons, Inc., New York **1986.**

[44] S. Pinchas, B. L. Silver, I. Laulicht, *J. Chem. Phys.* **1967**, *46*, 1506.

[45] H. J. Gehrke, J. Veal, *Inorg. Chim. Acta.* **1969**, *623*, 3.

[46] C. Knobler, B. R. Penfold, W. T. Robinson, C. J. Wilkins, S. H. Yong, *J. Chem. Soc. Dalton Trans.* **1980**, 248

[47] R. I. Buckley, R. J. H. Clark, *Coordin. Chem. Rev.* **1985**, *65*, 167.

[48] L. Seguin, M. Figlarz, R. Cavagnat, J. C. Lassègues, *Spectrochim. Acta.* **1995**, *51*, 1323.

[49] R. N. Hider, C. J. Wilkins, *J. Chem. Soc. Dalton Trans.* **1984**, 495.

[50] M. Nagano, M. Greenblatt, *J. Non-Cryst. Solids* **1988**, *101*, 255.

[51] R. Tokarz-Sobieraj, K. Hermann, M. Witko, A. Blume, G. Mestl, R. Schlögl, *Surf. Sci.* **2001**, *489*, 107.

[52] M. T. Greiner, M. G. Helander, Z. B. Wang, W. M. Tang, J. Qiu, Z. H. Lu, *Appl. Phys. Lett.* **2010**, *96*, 213302.

[53] P. A. Spevack, N. S. McIntyre, *J. Phys. Chem.* **1993**, *97*, 11020.

[54] S. O. Grim, L. J. Matienzo, *Inorg. Chem.* **1974**, *14*, 1014.

[55] H. You, Y. Dai, Z. Zhang, D. Ma, *J. Appl. Phys.* **2007**, *101*, 026105.

[56] K. Kanai, K. Koizumi, S. Ouchi, Y. Tsukamoto, K. Sakanoue, Y. Ouchi, K. Seki, *Org. Electron.* **2010**, *11*, 188.

[57] Irfan, H. J. Ding, Y. L. Gao, C. Small, D. Y. Kim, J. Subbiah, F. So, *Appl. Phys. Lett.* **2010**, *96*, 243307.

[58] J. Meyer, A. Shu, M. Kröger, A. Kahn, *Appl. Phys. Lett.* **2010**, *96*, 133308.

[59] W. Ma, C. Yang, X. Gong, K. Lee, A. J. Heeger, *Adv. Funct. Mater.* **2005**, *15*, 1617.

[60] W. Tress, K. Leo, M. Riede, *Adv. Funct. Mater.* **2011**, *21*, 2140.

[61] A. Wagenpfahl, D. Rauh, M. Binder, C. Deibel, V. Dyakonov, *Phys. Rev. B* **2010**, *82*, 115306.

www.MaterialsViews.com

ADVANCED
FUNCTIONAL
MATERIALS
www.afm-journal.de

FULL PAPER

[62] A. Kumar, S. Sista, Y. Yang, *J. Appl. Phys.* **2009**, *105*, 094512.

[63] J. Gilot, M. M. Wienk, R. A. J. Janssen, *Appl. Phys. Lett.* **2007**, *90*, 143512.

[64] C. S. Kim, S. S. Lee, E. D. Gomez, J. B. Kim, Y.-L. Loo, *Appl. Phys. Lett.* **2009**, *94*, 113302.

[65] G. Lakhwani, R. F. H. Roijmans, A. J. Kronemeijer, J. Gilot, R. A. J. Janssen, S. C. J. Meskers, *J. Phys. Chem. C* **2010**, *114*, 14804.

[66] C. M. Björström, S. Nilsson, A. Bernasik, A. Budkowski, M. Andersson, K. O. Magnusson, E. Moons, *Appl. Surf. Sci.* **2007**, *253*, 3906.

[67] T. Ishida, H. Kobayashi, Y. Nakato, *J. Appl. Phys.* **1993**, *73*, 4344.